Check for updates

ADVANCED MATERIALS
www.advmat.de

Cooperative Magnetic Interfacial Microrobot Couplefor Versatile Non-Contact Biomedical Applications

*Bowen Chen, Hao Wu, Yiyu Chen, Kangru Cheng, Ying Zhou, Juan Zhang, Chaowei Wang, Jiawen Li, Dong Wu, Jiaru Chu, and Yanlei Hu**

Magnetic interfacial microrobots are increasingly recognized as a promising approach for potential biomedical applications ranging from electronic functionalization to minimally invasive surgery and targeted drug delivery. Nevertheless, existing research faces challenges, including less cooperative interactions, contact-based cargo manipulation, and slow transport velocity. Here, the cooperative magnetic interfacial microrobot couple (CMIMC) is proposed to address the above challenges. The CMIMC can be maneuvered by a single magnet and readily switched between capture and release states. By leveraging cooperative interactions and meticulous engineering of capillary forces through shape design and surface treatment, the CMIMC demonstrates the ability to perform non-contact cargo manipulation. Using the synergy of preferred magnetization directions and magnetic field distribution, along with optimization of the resistance-reducing shape, the CMIMC significantly enhances the cargo transport velocity, reaching 12.2 body length per second. The studies demonstrate various biomedical applications like targeted drug delivery and myomectomy, paving the way for the broad implementation of interfacial microrobots in biomedical fields.

1. Introduction

In recent years, research on microrobots has emerged as a significant branch within the field of robotics, with its importance becoming increasingly prominent.[1–6] Currently, the majority of studies focus on microrobots operating in liquid or gas mediums, while research on microrobots at gas-liquid interfaces (e.g., air-water interface) is scarce. Interfacial microrobots, capable of manipulating microscopic objects at different gas-liquid interfaces, have great potential in cell manipulation,[7] drug delivery,[8] water treatment,[9–12] precision assembly,[13,14] and microelectronic pattern transfer.[15] Researchers have developed various strategies to propel interfacial microrobots, such as the Marangoni effect,[16–18] capillary forces,[14,19] electric fields,[20–22] light,[23–25] and magnetic fields.[26–30] Among these, magnetically driven interfacial microrobots are increasingly favored due to their pollution-free, remote, biocompatible, and untethered characteristics.[31–34] However, due to the global nature of magnetic fields, the microrobots within them are subjected to the same magnetic field effect, resulting in identical operational states. Therefore, multiple magnetic interface microrobots can only manipulate microscopic entities at the gas-liquid interface by pushing, lacking interactive capabilities (e.g., approaching each other for target capture), thereby failing to achieve efficient collaboration during the manipulation process. Several studies have explored the possibility of cooperative interactions among magnetic interfacial microrobots. For instance, Barbot et al. controlled the distance between the microrobots by adjusting the proximity of a permanent magnet to regulate the capture/release actions.[15] He et al. utilized a Helmholtz coil to generate an oscillating magnetic field, which controlled the approach and vibration of the microrobots, enabling both capture and cargo transport.[35] However, the studies lack design for the external shape and internal magnetic material distribution, resulting in slow cargo transport velocities of the magnetic interfacial microrobots (≈2 BL s^{-1}).[35] Additionally, the need for direct contact with the targeted cargo during the capture process confines their application prospects in the biomedical field. Consequently, it is imperative to devise a new cooperative magnetic interfacial microrobot that is capable of non-contact cargo manipulation while

B. Chen, H. Wu, K. Cheng, C. Wang, J. Li, D. Wu, J. Chu, Y. Hu
CAS Key Laboratory of Mechanical Behavior and Design of Materials
Key Laboratory of Precision Scientific Instrumentation of Anhui Higher Education Institutes
Department of Precision Machinery and Precision Instrumentation
University of Science and Technology of China
Hefei 230027, China
E-mail: huyl@ustc.edu.cn

Y. Chen
School of Manufacture Science and Engineering
Key Laboratory of Testing Technology for Manufacturing Process
Ministry of Education
Southwest University of Science and Technology
Mianyang 621010, China

Y. Zhou, Y. Hu
Department of Obstetrics and Gynecology
The First Affiliated Hospital of USTC
Division of Life Sciences and Medicine
University of Science and Technology of China
Hefei 230001, China

J. Zhang
Department of Mechanical Engineering
Tsinghua University
Beijing 100084, China

The ORCID identification number(s) for the author(s) of this article can be found under https://doi.org/10.1002/adma.202417416

DOI: 10.1002/adma.202417416

 © 2025 Wiley-VCH GmbH

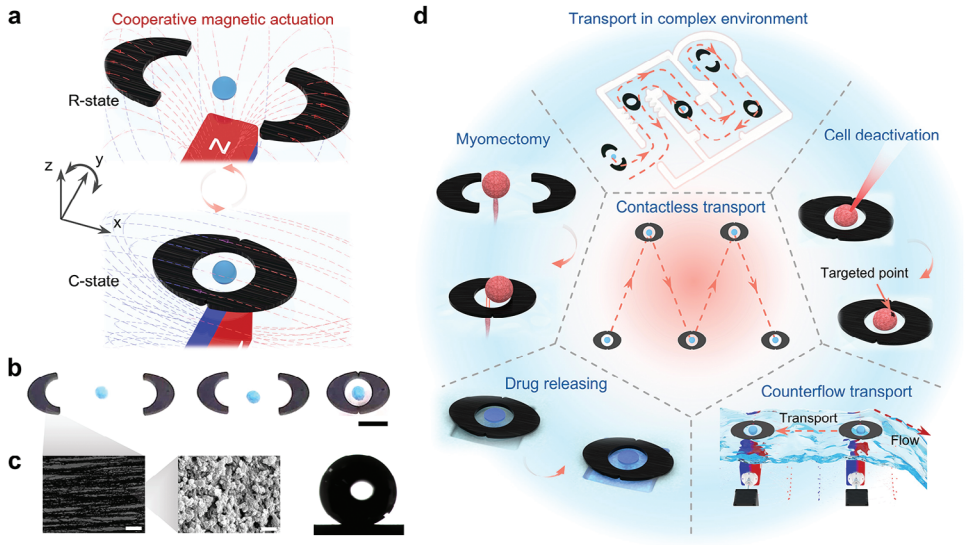

Figure 1. Schematic of multifunctional CMIMC. a) Schematic diagram illustrating the cooperative magnetic actuation of the cooperative magnetic interfacial microrobot couple (CMIMC) at the air-water interface. The diagram depicts the states of capture (C) and release (R) on an untethered cargo manipulated by an external magnet through rotational motion. b) Design and photographic images of the CMIMC capturing an untethered cargo driven by the magnet and capillary force at the air-water interface. Scale bar, 5 mm. c) Optical images of the CMIMC. From left to right: the internal carbonyl iron powder distribution, the surface microstructures, and the contact angle (154.5 ± 1.59 °), respectively. Scale bars, 300 and 2 μm, respectively. d) Schematic illustration detailing the diverse functions of the CMIMC commencing from the center and proceeding clockwise along the periphery. The CMIMC can achieve non-contact capture, transport, and release of an untethered cargo (Non-contact transport). Positioned at the top, the CMIMC can navigate in a complex environment for cargo transport (Transport in complex environment). Subsequently, the CMIMC can capture cell clusters and transport them to the target site for precise deactivation (Cell deactivation). The CMIMC further demonstrates the capability to transport cargo in counterflow environments (Counterflow transport). Positioned at the bottom, the CMIMC achieves targeted drug release in a disturbed environment (Drug releasing). The left image illustrates the CMIMC integrated with a ceramic blade for performing uterine fibroid excision. (Myomectomy).

ensuring both excellent controllability and high manipulation velocity.

Here, we have developed a new robotic system termed Cooperative Magnetic Interfacial Microrobot Couple (CMIMC). The CMIMC is composed of polydimethylsiloxane (PDMS) and carbonyl iron powder arranged in a specific chain distribution. By controlling the N-S orientation of a rectangular permanent magnet (i.e., simply rotating the magnet), we can switch the microrobot couple between capture/release states in 0.18/0.29 s, respectively. The CMIMC is capable of moving freely at the gas-liquid interface in both capture and release states by facilely adjusting the position of the permanent magnet. Optimized utilization of magnetic field and a streamlined shape design enable the CMIMC to achieve a high cargo transport velocity (12.2 BL s^{-1}). Additionally, the CMIMC can manipulate the targeted cargo based on capillary forces, avoiding direct contact with the cargo during the capturing, releasing, and moving processes, which significantly enhances its potential in biomedical applications. Owning to the distinctive properties of the CMIMC (cooperative interactions, non-contact cargo manipulation, and swift cargo transport), versatile applications, including non-contact counterflow targeted transport, precise deactivation of cell clusters, targeted drug release, and myomectomy procedures, have been demonstrated.

2. Results

2.1. Fabrication of Multifunctional and Cooperative CMIMC

The CMIMC consists of two components floating on the air-water interface, as illustrated in **Figure** 1a Each component can interact independently with the magnetic field generated by a permanent magnet positioned beneath the air-water interface. By rotating the magnet to change its *N-S* axis orientation, the CMIMC can flexibly transition between two stable equilibrium states, corresponding to the release state (R-state) and the capture state (C-state) (Figure 1a and Movie S1, Supporting Information). Furthermore, precise control of the CMIMC's position on the air-water interface is achieved through the 3D movement of the magnet. Therefore, by leveraging the state transition and position control, the CMIMC is capable of achieving some cooperative interactions, such as the capture, transport, and release of untethered floating cargo in synergy (Figure 1a,b).

For cooperative magnetic driving, each CMIMC component should respond differently to the same magnetic field to adjust its position while being able to react identically when needed to control the overall system. The CMIMC was made of polydimethylsiloxane (PDMS) mixed with superparamagnetic carbonyl iron powder, allowing it to respond to the magnetic

© 2025 Wiley-VCH GmbH

15214095, 0, Downloaded from https://advanced.onlinelibrary.wiley.com/doi/10.1002/adma.202417416 by University Of Science, Wiley Online Library on [21/02/2025]. See the Terms and Conditions (https://onlinelibrary.wiley.com/terms-and-conditions) on Wiley Online Library for rules of use; OA articles are governed by the applicable Creative Commons License

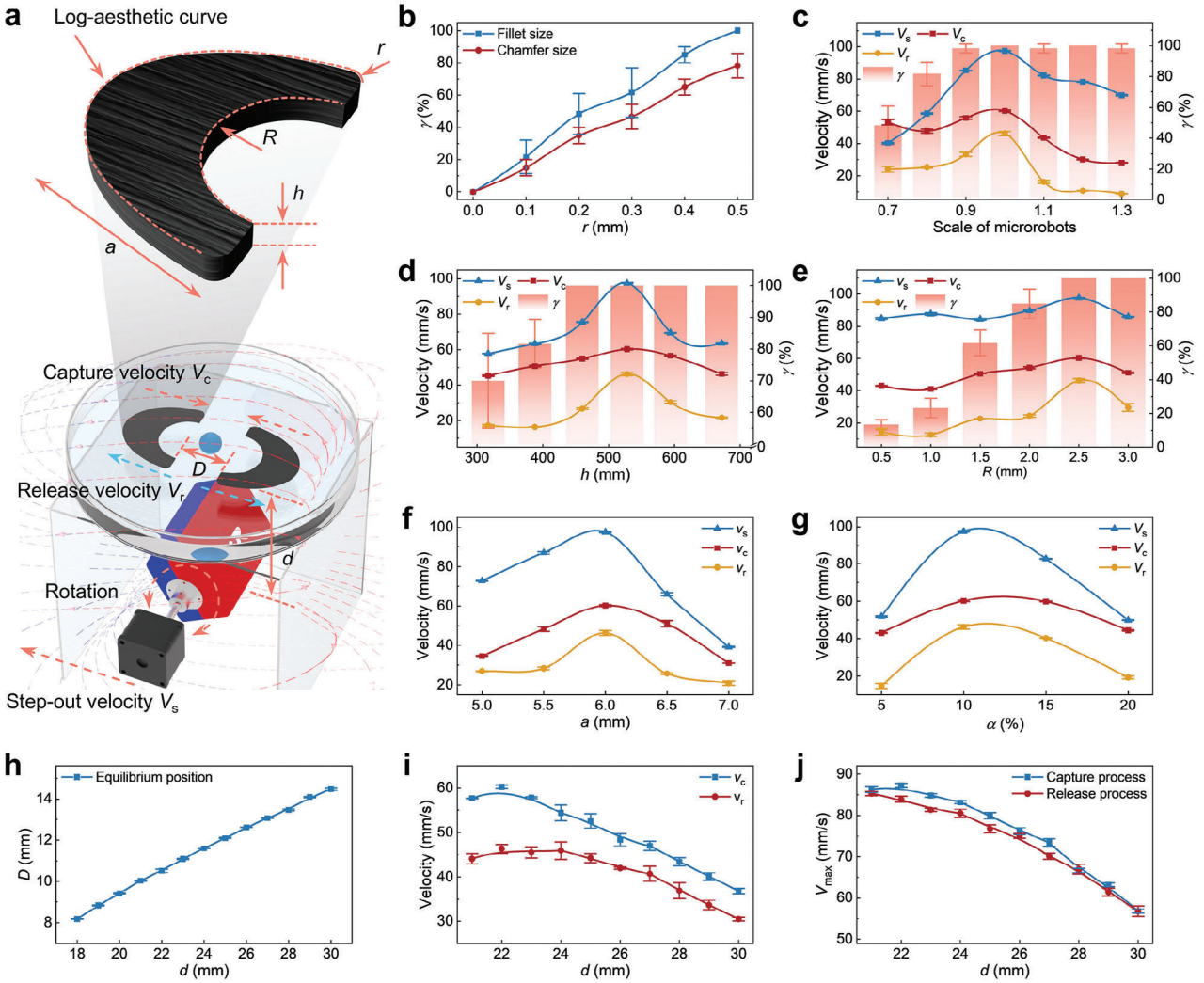

Figure 2. Characterization and performance of CMIMC under magnetic fields. a) Schematic of the experimental setup and identified parameters affecting the performance of the CMIMC. b–g) Selections of geometrical and material parameters for optimal capture velocity (V_c) ($n = 3$), release velocity (V_r) ($n = 3$), step-out velocity (V_s) ($n = 3$), and success ratio (γ) ($n = 60$) of transition from the capture state to release state. Parameters include fillet or chamfer sizes r (b), scale lengths (c), thicknesses h (d), cavity radii R (e), lengths a (f), and mass fraction of carbonyl iron powder α (g) of the CMIMC. Line graphs correspond to the left y-axis, and bar graphs correspond to the right y-axis in c to e. h) Equilibrium position with the distance between the driving magnet and the air-water interface. i,j) Average (i) and maximal (j) capture and release velocities (during the entire process) with the distance between the driving magnet and the air-water interface.

field for propulsion (Figure S1a, Supporting Information). We employed a spin coater to regulate the thickness of the carbonyl iron/PDMS mixture layer (Figures S1b and S2, Supporting Information). The 500 µm layer was placed above a permanent magnet to orientate the carbonyl iron powder inside the layer (Figure S1c, Supporting Information). Then, the layer was heated and cured to fix the spatial distribution of the carbonyl iron powder aligned along the nonhomogeneous magnetic field lines (Figures S1d and S3, Supporting Information).[36] Due to the anisotropic magnetic field distribution of the permanent magnet in space, different positions in the layer had different preferred magnetization directions, which could be preprogrammed by adjusting the distance between the layer and the magnet (Figure S4, Supporting Information). Finally, the layer was cut by the predetermined shape (resistance-reducing shape, **Figure 2a**) using a femtosecond laser, followed by surface modification treatment, resulting in a superhydrophobic CMIMC with preferred magnetization directions (Figure 1c and Figure S1e, Supporting Information). After the application of the driving magnetic field, the CMIMC tends to align the preferred magnetization directions with the magnetic field lines.[37] Thus, we can use this characteristic to control the relative position of the CMIMC to achieve cooperative magnetic driving. Moreover, introducing the preferred magnetization directions could enhance the magnetic induction during the response to the driving magnetic field, thereby increasing the magnetic driving force for the CMIMC (Figure S5, Supporting Information).[38,39]

During the transition from the R-state to the C-state, as the distance between the components decreases, capillary forces between the facing hydrophobic surfaces could facilitate automatic

© 2025 Wiley-VCH GmbH

15214095, 0, Downloaded from https://advanced.onlinelibrary.wiley.com/doi/10.1002/adma.202417416 by University Of Science, Wiley Online Library on [21/02/2025]. See the Terms and Conditions (https://onlinelibrary.wiley.com/terms-and-conditions) on Wiley Online Library for rules of use; OA articles are governed by the applicable Creative Commons License

alignment and self-assembly. This phenomenon arises from the mutual attraction of surfaces with identical hydrophilic or hydrophobic properties on a liquid interface, whereas surfaces with contrasting properties exhibit mutual repulsion.[13,14] Furthermore, the capillary force creates a "capillary potential well" within the internal cavities of the CMIMC. This potential well is a significant concept as it enables stable and non-contact capture, transport, and release of the cargo by providing a stable region for the cargo to reside within the cavity, thereby preventing the cargo from escaping.[40] As shown in Figure 1d, this non-contact transport, combined with the cooperativity of the components, enables multiple functionalities. First, we achieved non-contact targeted transport in complex environments through precise control of the movement paths of the CMIMC. Furthermore, combined with lasers, targeted precise deactivation of cell clusters was achieved. Following that, under conditions of enhanced magnetization and resistance-reducing shape, transport could even be achieved in counterflow environments. Subsequently, through drug encapsulation, targeted drug release in disturbed environments was achieved. Finally, by integrating a ceramic blade underneath the CMIMC and utilizing its high-velocity motion, a demo of myomectomy procedures was successfully performed, showcasing the versatility of the CMIMC.

2.2. Optimization of Shape and Parameters for CMIMC

Contemporary research on air-water interface microrobots is commonly encumbered by challenges such as sluggish propulsion velocities and suboptimal precision, markedly constraining their practical applications. The objective of the optimization is to maximize the separation success ratio (γ) and velocities of the CMIMC. The separation success ratio (γ) is the proportion of successful transitions from the C-state to the R-state through magnet rotation in experimental trials. The velocities include capture velocity (V_c), release velocity (V_r), and step-out velocity (V_s), which evaluate the cargo capture/release and the maximum transport velocities at the interface, respectively. These performance indicators are mainly determined by the driving force, resistance, and capillary force. The driving force exerted on the CMIMC by the external magnet is influenced by the mass concentration of carbonyl iron powder (α), the distribution of carbonyl iron powder (i.e., the shape of the CMIMC), and the distance (d) between the driving magnet and the air-water interface. The resistance and capillary force during the motions of the CMIMC are intricately linked to its geometric characteristics (Figure 2a). The complete experiment setup is shown in (Figure S6, Supporting Information). Accordingly, the characterization experiments focus on studying the effects of these factors on CMIMC's performance.

For the CMIMC's shape, we designed four types: triangular (i), circular (ii), rectangular (iii), and log-aesthetic curve (iv) (Figure S7, Supporting Information). Results in Figure S8a,b (Supporting Information), indicate that shape iv exhibited higher capture, release, and step-out velocities at the same feature size (f = 8 mm). To further validate the superior performance of shape iv, we designed a counterflow experimental environment with a controlled flow velocity. The microrobot was positioned at the air-water interface, and we gradually increased the water flow velocity until the microrobot could no longer maintain its stability at the interface. (Figure S9 and Movie S2, Supporting Information). As shown in Figure S8c (Supporting Information), shape iv was able to sustain stability in a higher water flow environment, reaching a velocity of up to ≈8.125 body length s^{-1} (BL s^{-1}, 65 mm s^{-1}, Movie S2, Supporting Information). This advantage stems from the log-aesthetic curve design, which minimizes resistance during motion.[41] Therefore, to enhance the motion efficiency, the contour design of the CMIMC was shaped as part of the logarithmic aesthetic (log-aesthetic) curve.

The key factor for a successful transition from the C-state to the R-state is whether the magnetic force on a CMIMC component along the x-axis could overcome the capillary force after rotating the magnet. In the C-state, the proximity of the CMIMC introduced sharp edges at the periphery, which hindered the entry of liquid into the contact area, consequently diminishing the success ratio. To enhance the stability of state transition, we designed the rounded edges at the contact edges to facilitate achieving the advancing angle (Figure 2a and Figure S10, Supporting Information).[42,43] A 100% success ratio (γ) was achieved when the radius of curvature (r) reached 0.5 mm, consistently outperforming chamfered edges, as shown in Figure 2b. Maintaining the curvature at 0.5 mm with an 8 mm baseline feature size, scaling up the CMIMC overall resulted in higher success ratios and the maximum velocities observed at the baseline feature size, as depicted in Figure 2c. This phenomenon arises because increasing the dimensions amplified magnetic force, as well as resistance and capillary forces. However, the rate of increase in capillary force was slower compared to the magnetic force (for more details, please refer to Supporting Information). Concurrently, diminishing the thickness (h) and expanding the cavity radius (R) of the CMIMC effectively decreased capillary resistance during separation, leading to an improved separation success rate, as illustrated in Figure 2d,e. Notably, the maximum velocities were attained at $R = 2.5$ mm and $h = 530$ µm. As observed in Figure 2f,g, both the length (a) of the captured log-aesthetic curve and the carbonyl iron powder concentration α exerted substantial influence on the CMIMC's performance. Optimal velocities were achieved at $a = 6$ mm and $\alpha = 10\%$, where separation success rates reached 100%. These results demonstrate that appropriate scaling, thinner thickness, and larger cavity radius can enhance CMIMC's performance.

Apart from the parameters of the CMIMC itself, the distance (d) between the driving magnet and the air-water interface also affects the CMIMC's performance. By adjusting the parameter d, the equilibrium separation of the CMIMC in the R-state can be modulated (Figure 2h). The closer proximity of the magnet to the CMIMC results in superior performance (Figure 2i,j). This phenomenon arises due to the amplified driving magnetic field, thereby engendering a heightened driving force. Nevertheless, excessively close distances significantly increase the magnetic force and torque in the z-direction, leading to an increased sinking depth (s) of the CMIMC (for more details, please refer to Supporting Information). This elevates resistance stemming from capillary and viscous forces, influencing the CMIMC's performance. Figure 2j illustrates the V_{max}, representing the peak velocity achieved during the capturing or releasing motion processes. Considering the combined relationship between velocities as described in Figure 2i,j and the distance (d), a distance of $d = 22$ mm was established as the default for subsequent experiments

© 2025 Wiley-VCH GmbH

15214095, 0, Downloaded from https://advanced.onlinelibrary.wiley.com/doi/10.1002/adma.202417416 by University Of Science, Wiley Online Library on [21/02/2025]. See the Terms and Conditions (https://onlinelibrary.wiley.com/terms-and-conditions) on Wiley Online Library for rules of use; OA articles are governed by the applicable Creative Commons License

unless otherwise specified. The CMIMC will undergo a process of acceleration followed by deceleration during the state transitions (Figure S11, Supporting Information). This behavior is attributed to the gradual decrease in the magnetic force component along the *x*-axis and the concurrent increase in resistance during the motions. Notably, capture velocity consistently surpassed release velocity owing to the distinct roles of capillary forces as driving and resisting factors in the two processes.

In this section, we have optimized the geometric parameters and experimental conditions for the CMIMC, resulting in a capture velocity of up to 7.5 BL s^{-1} (60.3 mm s^{-1}) and a maximum cargo transport velocity of 12.2 BL s^{-1} (97.5 mm s^{-1}). These velocities represent a leap forward, enabling non-contact and targeted transport over extended distances. To further assess CMIMC's stability, we conducted repetitive tests measuring the relative distances at equilibrium positions in both C and R states (Figure S12 and Movie S1, Supporting Information). Over 100 repetitions, CMIMC demonstrated robust consistency. These performance metrics underscore the broad potential applications of CMIMC in various domains.

2.3. Dynamics Mechanism of CMIMC

As shown in **Figure** 3a, during the motion of the CMIMC at the air-water interface, each component primarily experienced magnetic forces, capillary forces, gravity, and resistance from the water.[44–46] Due to the use of superparamagnetic materials, none of the components of the CMIMC retained residual magnetization (Figure S5, Supporting Information). Therefore, the magnetic moment of the CMIMC is entirely determined by the external magnetic field. This behavior is consistent with the principles of magnetic manipulation in solution, where the magnetic force must overcome hydrodynamic drag forces to enable controlled movement, as highlighted in studies on the magnetophoretic mobility of magnetic nanoparticles.[47] So, the magnetic force and torque acting on the CMIMC are:[15,47,48]

$$\mathbf{F}_B = \sum_i \nabla \left(\mathbf{m}_i \cdot \mathbf{B}_i\right) \tag{1}$$

$$\boldsymbol{\tau}_B = \sum_i \left(\mathbf{m}_i \times \mathbf{B}_i\right) \tag{2}$$

$$\mathbf{m}_i = \frac{V_i \chi}{2\mu_0} \mathbf{B}_i \tag{3}$$

where $\mathbf{m}_i$ represents the local magnetic moment of the CMIMC, $\mathbf{B}_i$ denotes the local magnetic field strength, $\mathbf{F}_B$ is the total magnetic force exerted on a single component of the CMIMC, V_i is the local volume of the CMIMC, $\boldsymbol{\tau}_B$ is the resulting torque, χ is the material magnetic susceptibility, and μ_0 is the vacuum magnetic permeability. Under the external magnetic field, the internal carbonyl iron powder distribution in the CMIMC tends to align with the field lines. By adjusting the distance between the driving magnet and the interface, the magnetic field distribution across the x-y plane could be modified, altering the equilibrium distance between the CMIMC (Figure 2h and Figure S13, Supporting Information). Due to the anisotropic distribution of the carbonyl iron powder and the irregular shape of the CMIMC, obtaining an analytical solution for the magnetic forces is challenging. Consequently, finite element analysis was used to calculate the magnetic forces acting on the CMIMC. Figure 3b,c and e,f depict the spatial distribution of the external magnetic field and the resultant magnetic force exerted on an individual component at the equilibrium positions in the R-state and the C-state, respectively. Owing to the non-uniform distribution of the driving magnetic field, the magnitude of magnetic forces acting on the CMIMC varied continuously as they moved relative to the driving magnet. Moreover, initially subdued, the magnetic interaction force ($\mathbf{F}_{Bij}$) between the CMIMC experienced substantial amplification as they approached proximity. This result was rigorously validated through simulations. Figure 3d,g depicts the variations in magnetic forces along the *x*-axis acting on a single component, with respect to the relative distance (D) between the CMIMC during the transition to the R-state and the C-state, respectively. The simulated equilibrium position (D = 10.5 mm) in the R-state corresponds closely with the experimentally measured (D = 10.7 mm) at a magnet-interface distance of d = 22 mm (Figures 2h and 3d). The magnetic forces along the *z*-axis acting on the CMIMC are shown in Figure S14 (Supporting Information).

Due to surface tension at the air-water interface, each component of the CMIMC is subject to capillary forces. The key to determining the capillary forces acting on the CMIMC lies in building the contour functions of the merged meniscus (surface between the couple) and the single meniscus (log-aesthetic curved surface). During assembly, the merged meniscus undergoes continuous variation with the relative distance (D) between the CMIMC, whereas the single meniscus remains nearly constant. This results in the angles θ and θ' between the capillary forces and the horizontal direction varying as functions of D and remaining constant, respectively. The detailed calculation process of θ and θ' is presented in Supporting Information. Thus, the capillary force acting on a single component is:

$$\mathbf{F}_C = \sum_i \gamma L_{mi} \mathbf{k}_{mi} + \sum_j \gamma L_{sj} \mathbf{k}_{sj} \tag{4}$$

where γ is the surface tension of the water, L_{mi} and L_{sj} denote the local three-phase contact lines of the merged meniscus and single meniscus, respectively, $\mathbf{k}_{mi}$ and $\mathbf{k}_{sj}$ are their corresponding unit direction vectors corresponding with θ and θ'. If the CMIMC is assumed to maintain equilibrium in the vertical direction, as given by:

$$\mathbf{G} + \mathbf{F}_{Bz} + \mathbf{F}_{Cz} = 0 \tag{5}$$

where $\mathbf{G}$, $\mathbf{F}_{Bz}$, and $\mathbf{F}_{Cz}$ are the gravitational force, magnetic force in the z-direction, and capillary force in the z-direction acting on each microrobot, respectively. Given the gravitational and magnetic forces, the bottom of the CMIMC will submerge to a specific distance *s* relative to the interface, as depicted in Figure S15 (Supporting Information). Calculations confirm that the magnetic force will not exceed the capillary force in the z-direction, preventing the CMIMC from sinking to the bottom of the water (Figure S15, Supporting Information).[49,50] The resistance and capillary force in the x-direction vary with different sinking depths, as illustrated in Figure 3h,i, respectively. The computed

© 2025 Wiley-VCH GmbH

15214095, 0, Downloaded from https://advanced.onlinelibrary.wiley.com/doi/10.1002/adma.202417416 by University Of Science, Wiley Online Library on [21/02/2025]. See the Terms and Conditions (https://onlinelibrary.wiley.com/terms-and-conditions) on Wiley Online Library for rules of use; OA articles are governed by the applicable Creative Commons License

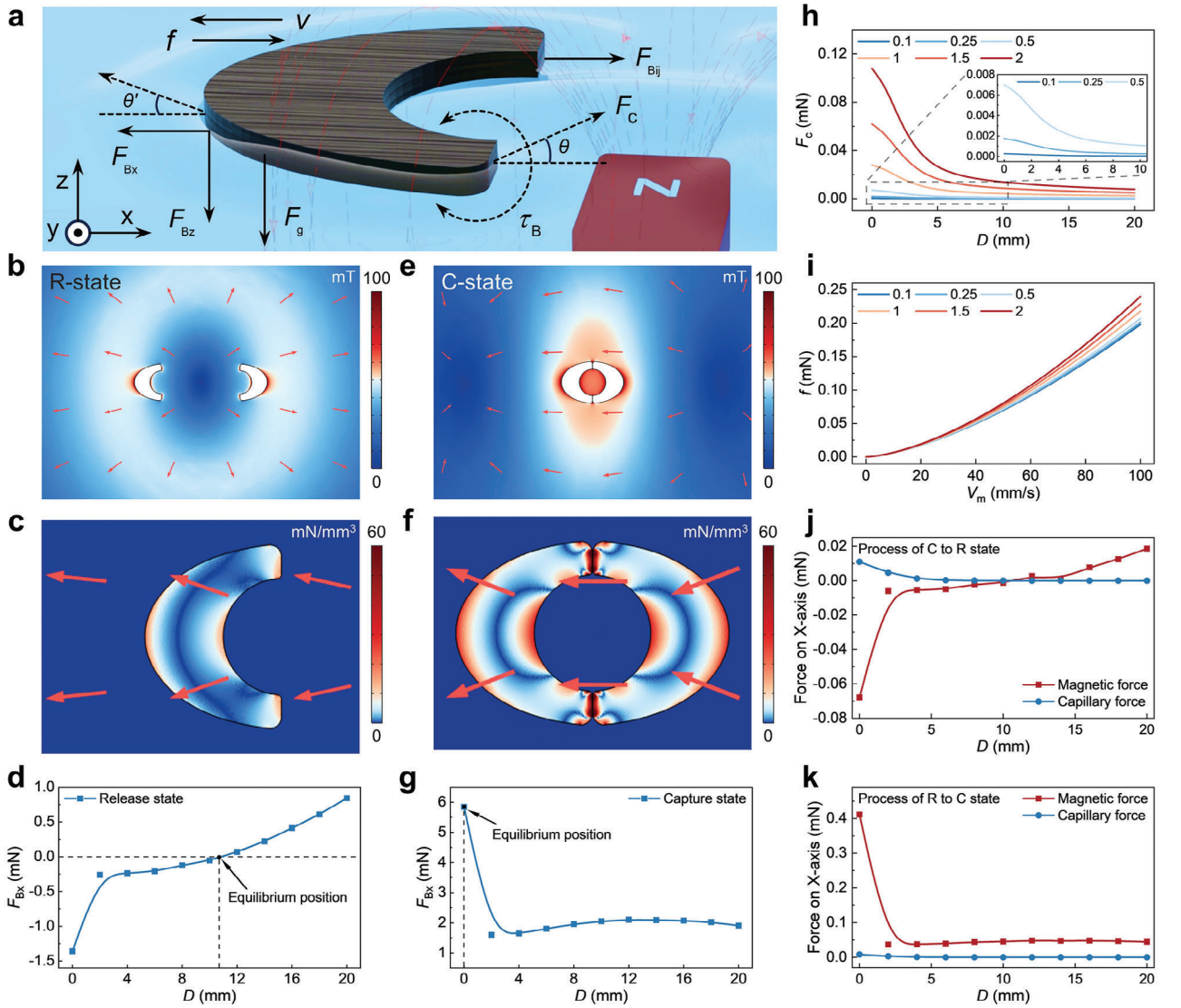

Figure 3. Rough calculation and simulation of the magnetic fields and forces during motions. a) Schematic illustration of the forces and torques acting on a single component of the CMIMC. The capillary force (F_c) is determined by the single and merged menisci at the three-phase contact lines, which depend on the angles (θ' and θ) between the menisci and the horizontal direction as the distance (D) between the CMIMC changes. F_{Bx}, F_{Bz}, and τ_B represent the magnetic force components along the x, z-axes, and the magnetic torque exerted by the external magnet, respectively. F_{Bij} denotes the magnetic interaction force between the CMIMC. F_g is the gravitational force. b,e) Simulated background magnetic field distributions in the R-state (b) and C-state (e). The arrow's direction indicates the direction of the magnetic field at that location, and the length indicates the magnitude. c,f) Simulated magnetic force density distributions of the CMIMC in the R-state (c) and C-state (f), with the red arrow indicating the direction of the magnetic field at that location. d,g) Magnetic force components along the *x*-axis as a function of distance (D) in the R-state (d) and C-state (g). The equilibrium positions for both states are marked. h) Calculated capillary forces of the CMIMC as a function of distance (D) at varying distances (s) from the air-water interface. i) Calculated viscous resistance of the CMIMC as a function of their velocity at varying distances (s) from the air-water interface. j,k) Comparative analysis of magnetic and capillary forces along the *x*-axis during the transitions from C to R-state (j) and R-state to C-state (k), respectively.

capillary forces along the *x*-axis for an individual component are ≈7 μN (at the equilibrium position in the C-state) and 1.8 μN (at the equilibrium position in the R-state). At the maximum velocity (97.5 mm s^{-1}) of cargo transport, an individual component of CMIMC experiences a resistance force of ≈0.169 mN. These calculations are predicated on $s = 0.5$ mm.

Without considering CMIMC tilting, the horizontal motion of the CMIMC in the experimental investigation was examined, which is given by:

$$m\frac{\partial^2 \mathbf{v}}{\partial t^2} = \mathbf{F}_{Cx}(D, s) + \mathbf{f}(\mathbf{v}, s) + \mathbf{F}_{Bx}(D) + \mathbf{F}_{Bij}(D) \quad (6)$$

where m is the mass of an individual component (≈0.01 g), $\mathbf{v}$ is the current velocity of the component, and $\mathbf{F}_{Cx}$ and $\mathbf{F}_{Bx}$ are the capillary force and magnetic force exerted on the component in the x-direction, respectively. In practical computations, appropriate handling of the simulated magnetic forces was performed. The components of magnetic and capillary forces exerted along

© 2025 Wiley-VCH GmbH

15214095, 0, Downloaded from https://advanced.onlinelibrary.wiley.com/doi/10.1002/adma.202417416 by University Of Science, Wiley Online Library on [21/02/2025]. See the Terms and Conditions (https://onlinelibrary.wiley.com/terms-and-conditions) on Wiley Online Library for rules of use; OA articles are governed by the applicable Creative Commons License

the x-axis on the CMIMC, sinking depth s, θ and θ' during the state transitions were determined using the equations mentioned above (Figure 3h,k, and Figure S15, Supporting Information). Initially, the separation force (resultant force combining magnetic force and capillary force) provided at the starting position amounted to ≈56.8 μN and decreased to zero as the distance between the CMIMC increased until reaching the equilibrium position at the R-state, where $D = 10.7$ mm, consistent with experimental measurements (Figure 2h). Moreover, when the CMIMC is at the equilibrium position in the R-state and C-state, it is characterized by a stable state that allows it to restore its equilibrium position and maintain stability against external perturbations. Besides, during the transition of the CMIMC from the R-state to the C-state, the magnetic and capillary forces act coherently due to mutual attraction between surfaces of similar hydrophilicity, serving as driving forces. Consequently, throughout the capture process, the driving force remained consistently positive until CMIMC made contact (Figure 3k). The theoretical examination based on preferred magnetization directions substantiates the feasibility of controlling the relative distance of the CMIMC using a permanent magnet. Derivations and detailed calculations are presented in the Supplementary Information.

2.4. Targeted Transport in Complex Environments

After optimizing the motion performance and analyzing the dynamics mechanism, we explored the extensive potential applications of the CMIMC based on cooperative interactions. Because the geometric center axis of the CMIMC consistently aligned with that of the driving magnet, it enabled proximity to the untethered cargo floating at the interface. When the cargo was positioned at the center of the CMIMC's cavity, the driving magnet was rotated using a motor to align its N-S axis with the x-axis, switching the CMIMC to the C-state and enabling non-contact capture of the untethered cargo. Due to the influence of capillary forces, there was a continual mutual repulsion between the cargo and CMIMC. Furthermore, owing to the presence of the capillary potential well, the cargo consistently resided within the cavity's center of the CMIMC. Consequently, throughout the entire process of capture, transport, and release, the object remained in a state of non-contact with the CMIMC, which is currently difficult to achieve in research endeavors. This precise manipulation of the CMIMC's position at the interface enabled non-contact targeted transport of the cargo. Upon reaching the predetermined position, the driving magnet was rotated again to switch the CMIMC to the R-state, allowing for the non-contact release of the cargo (**Figure** 4a and Movie S3, Supporting Information).

In experimental settings, we directed the motion of the CMIMC with a stepping motor and an XYZ 3D displacement stage (Figure S6, Supporting Information), ensuring exact real-time and pre-programmed positional control and reliable state transitions. Figure 4b illustrates the CMIMC approaching and capturing an untethered cargo on the air-water interface with high precision. Subsequent manual manipulation facilitated targeted transport and release, concluding with the CMIMC retrieval along the original path. Additionally, in a large spatial area, we validated the manual capture of the untethered cargo at the interface, followed by automatic transport and release along predetermined paths. Circle-shaped and letters-shaped tracks were demonstrated in experiments, as shown in Figure 4c,d, respectively (Movie S3, Supporting Information).

Based on the validations mentioned above, our CMIMC exhibits the cooperativity to capture an untethered cargo and conduct targeted transport along arbitrary trajectories. Furthermore, we performed experimental validation using cabbage seeds to showcase CMIMC's programmable motion capabilities to explore more complex environments and potential applications in site-directed biological culture (Figure S16, Supporting Information). Initially, we used the CMIMC to capture a seed. Then, we transported the CMIMC to the targeted position, navigating through a complex environment for designated cultivation periods, and subsequently retrieved the CMIMC. Comparative experiments involving cabbage seeds cultivated in water, with and without CMIMC manipulation in different conditions, demonstrated the feasibility and effectiveness of the CMIMC for site-directed biological culture in a disturbed environment (Figure S16 and Movie S4, Supporting Information). Simultaneously, co-cultivation for ≈19 h confirmed the CMIMC's non-toxicity. By leveraging its non-toxicity, flexible cooperativity, and ability to maintain cargo integrity without direct contact, we advanced its potential in biotechnology. We have established a laser irradiation point with predetermined coordinates at the interface for cellular deactivation. By capturing yeast cell clusters and subsequent laser activation, we further demonstrated the precise targeted transport capability of the CMIMC. Using the CMIMC, we captured the yeast cell clusters, transported them along the designated path to the deactivation coordinates, activated the laser upon reaching the target position, and transported them out of the system. The control experiment, without laser activating, confirmed that the CMIMC did not impact cell viability. The viability of the clusters was ≈15.6% after the laser irradiation, compared to near 100% viability for sole transport, which corroborates the biocompatibility of the CMIMC (Figure S17 and Movie S5, Supporting Information). For more details, please refer to the Experimental Section.

2.5. Targeted Drug Transport and Myomectomy

After confirming the biocompatibility of the CMIMC, we subsequently investigated its diverse cooperative applications in biomedicine. We first explored the application prospect of the CMIMC for targeted drug transport and release in an anatomical model of the human stomach. The capability to achieve disturbance-resistant targeted drug release positioned the CMIMC as a promising platform for precise drug delivery to gastric ulcers. Active targeted delivery with site-directed drug release can reduce dosage and prevent side effects of drugs. **Figure** 5a schematically illustrates the experimental process, which can be roughly divided into three stages: pushing a medical catheter (Stage I), deploying the drug-loaded CMIMC using an external magnet through the catheter (Stage II), releasing the drug at the targeted position and retrieving the CMIMC by the catheter (Stage III). Snapshots of the experimental process are shown in Figure 5c, progressing from left to right. Initially, only an ex vivo stomach model containing an appropriate volume of fluid to simulate a realistic gastric environment was present (0 s).

© 2025 Wiley-VCH GmbH

15214095, 0, Downloaded from https://advanced.onlinelibrary.wiley.com/doi/10.1002/adma.202417416 by University Of Science, Wiley Online Library on [21/02/2025]. See the Terms and Conditions (https://onlinelibrary.wiley.com/terms-and-conditions) on Wiley Online Library for rules of use; OA articles are governed by the applicable Creative Commons License

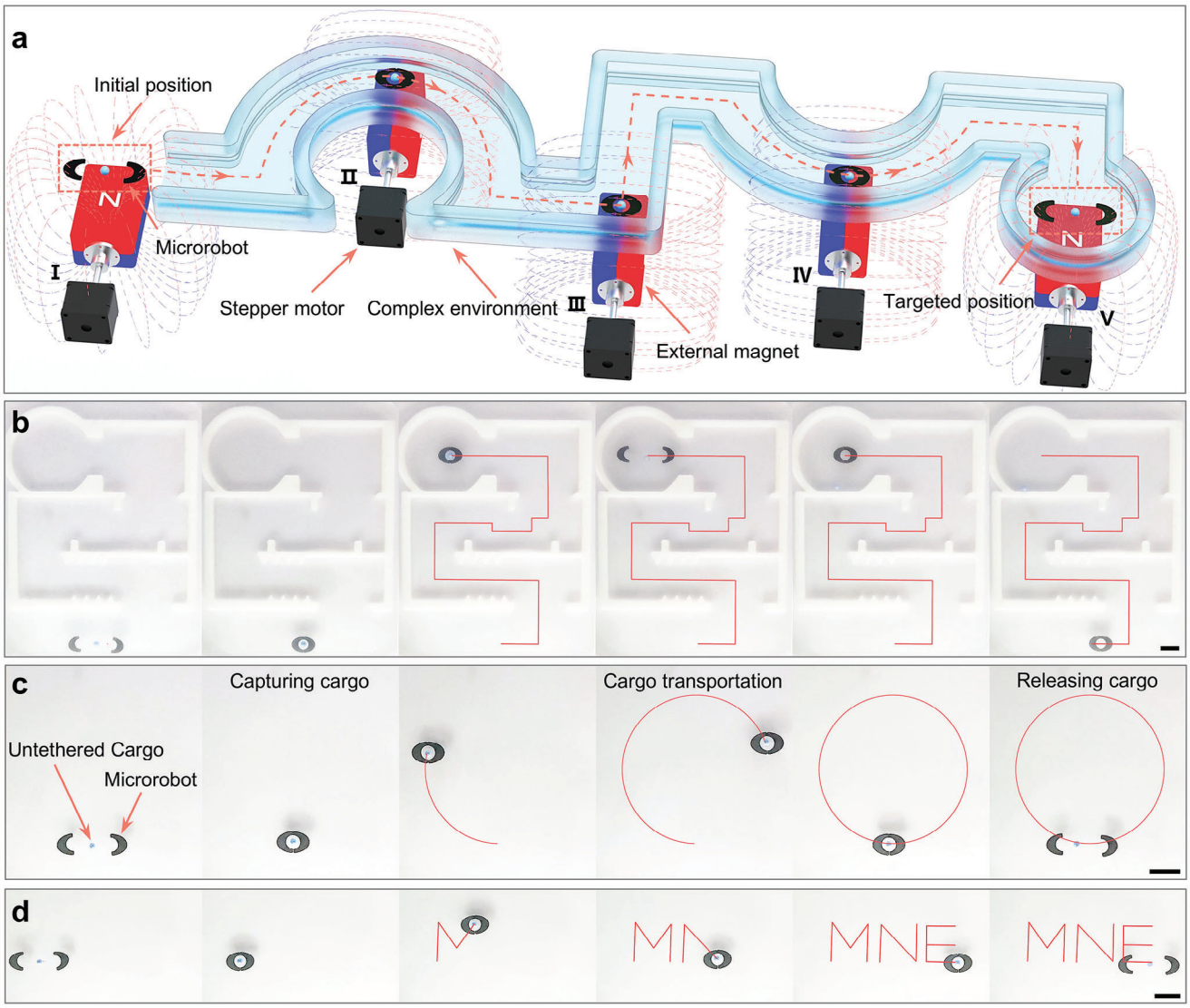

Figure 4. Non-contact and cooperative targeted transport. a) Illustration depicting the non-contact and cooperative transport of an untethered cargo by the CMIMC at the air-water interface, navigating through a complex environment. b–d) Non-contact targeted cargo transport demonstrations by the CMIMC with different route shapes, complex-shaped (b), circle-shaped (c), and letters-shaped (d) trajectories. Scale bar, 10 mm.

Subsequently, a medical catheter and the CMIMC loaded with drugs were deployed (23 s), followed by a continuous process of targeted drug release (340 s). As a demonstration, a biocompatible dye, specifically an edible pigment, was utilized for drug staining, which was encapsulated within the hydrogel. The retrieval of the CMIMC and catheter was completed following prolonged drug release (692 s). As a control experiment, Figure 5d shows the situation of targeted drug release without CMIMC capture. In this scenario, apart from the challenge of the drug reaching the targeted position, disturbances such as external vibrations and the Marangoni effect induced by concentration gradients could cause the drug to deviate from the targeted site, thereby reducing treatment efficacy (Movie S6, Supporting Information). Figure 5b presents the drug concentrations released under tethered and untethered conditions in Figure 5c,d. Additional control groups included drug concentration not collected (Control I) and drug concentration collected away from the ulcer site (Control II). The method employed for determining drug concentration involved collecting solution from a specific site, evaporating the solvent through heating, and assessing the change in container mass before and after collection to quantify drug concentration. Minimal concentration changes were noted when only heating the containers and distant from the targeted position. Moreover, the concentration at the targeted position following drug release with the CMIMC was 1.72-fold higher compared to the non-CMIMC condition (Figure 5b). This significant increase in drug concentration at the targeted position demonstrates the potential of the CMIMC in enhancing drug efficacy (for more details, see Experimental Section).

Furthermore, we also explored the application prospect of the CMIMC in myomectomy. It is typically essential to achieve uterine distension before performing myomectomy by instilling an

© 2025 Wiley-VCH GmbH

15214095, 0, Downloaded from https://advanced.onlinelibrary.wiley.com/doi/10.1002/adma.202417416 by University Of Science, Wiley Online Library on [21/02/2025]. See the Terms and Conditions (https://onlinelibrary.wiley.com/terms-and-conditions) on Wiley Online Library for rules of use; OA articles are governed by the applicable Creative Commons License

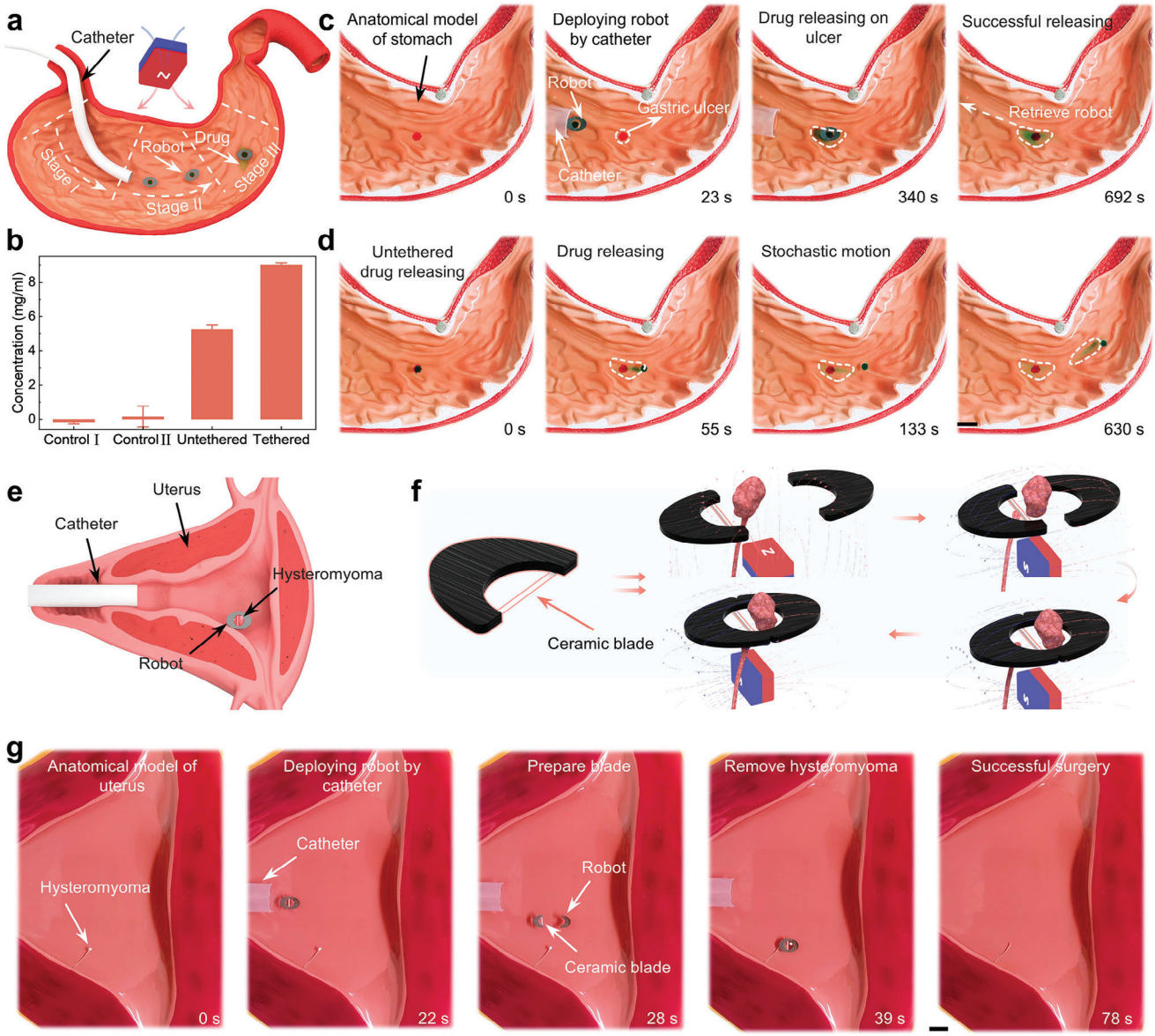

Figure 5. Functional demonstration of targeted drug delivery, release, and myomectomy. a) Conceptual schematic depicting the drug delivery process of the CMIMC inside a stomach filled with some gastric acid, which involves three stages: pushing a medical catheter, deploying the CMIMC by the catheter, and drug releasing. b) Drug concentrations are measured by the variation in the mass of the container, which underwent processes of solution filling and subsequent drying ($n = 5$). Control I, only the container is heated, and control II is the solution distant from the ulcer. c) Targeted drug delivery is demonstrated in an anatomical stomach model using a magnet and drug releasing on the ulcer using the CMIMC. d) An untethered drug is released on the ulcer site with stochastic motion. e) Conceptual schematic depicting the myomectomy process of the CMIMC inside a uterus filled with some water. f) Schematic illustration of the CMIMC composited with a ceramic blade and the myomectomy process. g) Myomectomy is demonstrated in an anatomical uterus model, involving three stages: pushing a medical catheter, deploying the CMIMC by the catheter, and removing the hysteromyoma. Scale bar, 10 mm.

appropriate volume of fluid and creating an air-water interface within the uterine cavity, which is consistent with the working condition (air-water interface) of the CMIMC. Figure 5e depicts a schematic diagram illustrating the excision of a uterine fibroid using our CMIMC. We coupled a ceramic blade at the bottom of the CMIMC to excise fibroids, as shown in Figure 5f. Utilization of a ceramic blade over a metallic counterpart aimed to mitigate susceptibility to external magnetic field interference.

Figure 5f schematically delineates the experimental procedure, which could be roughly divided into three sequential stages: pushing a medical catheter (Stage I), deploying the CMIMC in the C-state to the targeted fibroid for excision, transitioning to the R-state to position the fibroid adjacent to the blade (Stage II), reverting to the C-state to execute fibroid excision, and finally retrieving both the excised fibroid and the CMIMC using the catheter (Stage III). Snapshots depicting the experimental

© 2025 Wiley-VCH GmbH

15214095, 0, Downloaded from https://advanced.onlinelibrary.wiley.com/doi/10.1002/adma.202417416 by University Of Science, Wiley Online Library on [21/02/2025]. See the Terms and Conditions (https://onlinelibrary.wiley.com/terms-and-conditions) on Wiley Online Library for rules of use; OA articles are governed by the applicable Creative Commons License

process are illustrated in Figure 5g, progressing sequentially from left to right. Initially, a physiologically realistic ex vivo uterine model filled with an appropriate volume of fluid and a designated fibroid for excision was presented (0 s). Subsequently, a medical catheter and the CMIMC in the C-state were deployed (22 s). Utilizing a driving magnet, the CMIMC approached the targeted fibroid, thereby transitioning into the R-state (28 s) and continuing in the R-state and approaching the targeted fibroid, bringing it into proximity to the blade. By rotating the magnet, the CMIMC reverted to the C-state, utilizing its high capture velocity to complete the excision (39 s). The uterine fibroid was successfully excised, and the myomectomy surgery was successfully performed. The excised fibroid and CMIMC were then retrieved using the catheter (78 s) (Movie S7, Supporting Information). Furthermore, we demonstrated that CMIMC exhibits high motion performance in different fluids, further validating its feasibility for targeted drug delivery in a stomach and myomectomy (Figure S18, Supporting Information). For detailed experimental procedures, please refer to the Experimental Section.

3. Conclusion

In summary, we proposed the CMIMC for versatile biomedical applications. To achieve precise control and flexible cooperativity of the CMIMC, we mixed the carbonyl iron powder with a PDMS matrix and engineered the preferred magnetization directions to ensure optimal responsiveness to the external magnetic field. A permanent magnet was used to control the position and equilibrium states of the CMIMC at the air-water interface. Combined with capillary effects, we realized non-contact capture, transport, and release of untethered floating cargo through the cooperative interactions of the CMIMC. Through the deliberate design of the CMIMC's shape and geometric parameters, we optimized its locomotion performance. The maximum cargo transport velocity was achieved at 12.2 BL s^{-1}. We also conducted counterflow experiments to validate its disturbance resistance capability, achieving stable transport in a counterflow environment at a velocity of 8.1 BL s^{-1}. Repetitive state-transition experiments were performed to confirm its robustness. Additionally, simulations of the driving magnetic field and magnetic forces on the CMIMC were conducted to reveal the underlying mechanisms of its cooperative motion. Moreover, we validated the precise and flexible cooperative interactions of the microrobot couple through transport experiments in complex-shaped, circle-shaped, and letters-shaped trajectories, respectively. Real-time motion control and state transitions were demonstrated, as well as transport along predefined trajectories. Furthermore, we showcased the control precision and biocompatibility of the CMIMC control through cabbage seed hydroponics and targeted deactivation of yeast cell clusters. Finally, the potential applications of the CMIMC in the biomedical field were demonstrated. Its capability for targeted drug release in an ex vivo stomach model was verified, achieving a drug concentration increase of 1.72-fold higher compared to the non-CMIMC clamping condition. In an ex vivo uterine model, we successfully performed the removal of uterine fibroids by combining the CMIMC with a ceramic blade by leveraging its high-velocity capture and flexible manipulation capabilities.

4. Experimental Section

Carbonyl Iron/PDMS Mixture Layer Fabrication: Polydimethylsiloxane (PDMS, Sylgard 184, Dow Corning) as the matrix material of the CMIMC was used, mixed with PDMS curing agent and carbonyl iron powder (particle diameter 3–5 µm, ≥99.5% purity, Nangong Rui Teng Alloy Material Co., Ltd.). Initially, these constituents were blended in a mass ratio of 10:1:1 and thoroughly mixed using manual agitation with a glass rod to ensure uniform distribution. Subsequently, the mixture underwent 15 min of vacuum degassing to eliminate entrapped air bubbles. After degassing, the mixture was cast onto the center of a clean glass slide (70×70×1.1 mm). The glass slide was then subjected to spin-coating on a spin coater (Opticoat MSA100, Mikasa Co. Ltd., Japan) at 150 rpm for 40 s to achieve a uniform layer. The coated glass slide, with a mixture layer thickness of ≈500 µm, was transferred into a custom-built curing mold made of laser-cut wooden material to minimize magnetic field interference. Positioned beneath the center of the glass slide, at ≈35 mm distance, was a neodymium-iron-boron (NdFeB) permanent magnet (N52, 25×25×25 mm), with its *N-S* axis parallel to the glass surface. This corresponded to a magnetic field magnitude of ≈8 mT, which effectively aligned the carbonyl iron powder into lines along the magnetic flux lines. Then, the entire mold assembly was placed in an oven and cured at 65 °C for 1.5 h. This curing process facilitated the alignment of the carbonyl iron powder along the magnetic flux lines induced by the magnet, resulting in the desired microstructure formation within the composite material.

Femtosecond Laser Fabrication: The femtosecond laser system based on the Ti: sapphire femtosecond laser system (80L8TICEACE-100F-1K, Spectra-Physics Solstice Ace, USA) was employed for precise cutting and modification of the carbonyl iron/PDMS mixture layer. The laser beam features included a pulse width < 100 fs, a repetition rate of 1 kHz, and a central wavelength of 808 nm. This beam was directed through a scanning system (model s-9210d, Sunny Technology, China) and focused onto the magnetic film using an F-theta lens with a focal length of ≈63 mm. The scanning path and velocity were controlled by the scanning system, and the laser power was adjustable via an optical attenuator. Cutting operations utilized a scanning power of 600 mW and a speed of 2 mm s^{-1}, repeated 15 times. Then, orthogonal crossed line-by-line consecutive scanning was performed on both the upper and lower surfaces of CMIMC to create the surface microstructures. The process employed an optimized laser power of 450 mW, a scanning speed of 12 mm s^{-1}, and a line spacing of 0.03 mm.

Characterization: The surface microstructures of CMIMC were characterized by a scanning electron microscope (ZEISS EVO18). The contact angle and advancing angle of the MIM were measured by the contact angle system (CA-100C, Shanghai Innuo Precision Instruments Co., Ltd) at ambient temperature. Measures were conducted on three different samples. The volume of the test droplets was ≈4 µL generated by a syringe. The optical image and the advancing process were recorded by a charge-coupled device (CCD) of the contact angle system.

CMIMC Manipulation: Throughout all experiments, the orientation of the CMIMC was controlled by a permanent magnet (N25, 25×25×40 mm) positioned directly underneath the interface. The magnet was securely mounted on a stepper motor (42BYGH34, Yi Xing Technology Co., Ltd, China), which was operated via an Arduino UNO R3. Rotation of the stepper motor, and thus adjustment of CMIMC's equilibrium state, was achieved remotely using an infrared receiver module and an infrared remote control unit (Keyes). The stepper motor assembly was affixed to a precision 3D displacement stage (X-XYZ-LSM200A, Zaber Technologies Inc.), offering a travel range of 20 cm.

Yeast Cell Culture: Yeast cells were cultured on YPD solid medium (1% yeast extract, 2% peptone, 2% glucose, 1.5% agar, sourced from Shanghai Ruichu Biotech Co., Ltd.). The yeast cells were incubated at a constant temperature of 30 °C for 2–3 days. Subsequently, the yeast cells were transferred to a YPD liquid medium (1% yeast extract, 2% peptone, 2% glucose). A 5% mass fraction of glucose was added to the liquid medium to facilitate the transport of yeast cells.

Yeast Cell Viability Experiment: An infrared laser was used for deactivation (808 nm, 300 mW, Shenzhen Infrared Laser Technology Co., LTD,

© 2025 Wiley-VCH GmbH

15214095, 0, Downloaded from https://advanced.onlinelibrary.wiley.com/doi/10.1002/adma.202417416 by University Of Science, Wiley Online Library on [21/02/2025]. See the Terms and Conditions (https://onlinelibrary.wiley.com/terms-and-conditions) on Wiley Online Library for rules of use; OA articles are governed by the applicable Creative Commons License

China). A 4% stock solution of trypan blue was first prepared. 4 g of trypan blue (BASF SE) was weighed and ground with a small amount of distilled water. Water was added to make up the volume to 100 mL, and the solution was filtered using filter paper and stored at 4 °C. The yeast cell suspension was mixed with a 0.4% trypan blue solution (diluted in PBS). The cells were observed under a microscope (Leica DM IL LED, Leica Microsystems), and viability was calculated. Dead cells were stained blue, while live cells remained colorless and transparent.

Ex Vivo Experiments: In Figure 4b, Figures S9, S16 and S17 (Supporting Information), the models utilized were fabricated using a 3D printer (Dreamer NX, Zhejiang Flashforge 3D Technology Co., LTD) with polylactic acid (PLA) as the material. The models and the catheter in Figure 5c,d, and g were purchased from Taobao, China. For targeted drug transport experiments, the drug (Omeprazole Enteric-coated Tablets) was adsorbed by porous hydrogels. The drugs were stained using edible dyes, and the hydrogels were polymerized under UV exposure. Drug concentrations were assessed by measuring changes in mass using centrifuge tubes. Initially, some solutions were loaded into the centrifuge tubes. Then, the centrifuge tubes were heated to evaporate the water. Finally, the mass changes were measured. Measures were conducted on three different samples. In the myomectomy simulation, a plastic ball simulated uterine fibroid and was affixed to the uterine model using tape. The ceramic blade was adhered underneath the CMIMC using adhesive.

Supporting Information

Supporting Information is available from the Wiley Online Library or from the author.

Acknowledgements

The authors acknowledge the Experimental Center of Engineering and Material Sciences at USTC for the fabrication and measuring of samples. This work was partly carried out at the USTC Center for Micro and Nanoscale Research and Fabrication. The authors also acknowledge L. O., professor of the Department of Mechanical Engineering at Tsinghua University, for participating in the discussion of experimental methods. This work was supported by the National Key Research and Development Program of China (2024YFB4610700, 2021YFF0502700), National Natural Science Foundation of China (Nos. 52122511, 52375582, 62405307, and U20A20290), Anhui Provincial Natural Science Foundation (2308085QF218), China National Postdoctoral Program for Innovative Talents (BX20230351), China Postdoctoral Science Foundation (2023M733382), Major Scientific and Technological Projects in Anhui Province (202203a05020014), Fundamental Research Funds for the Central Universities (WK5290000004 and WK2090000058), Youth Innovation Promotion Association CAS (Y2021118).

Conflict of Interest

The authors declare no conflict of interest.

Author Contributions

B.C. and H.W. contributed equally to this work. B.C., H.W., and Y.H. conceived the idea and designed the project; B.C., H.W., Y.C., K.C., Y.Z., J.Z. and C.W. performed all the experiments; B.C. performed the characterization; B.C. and H.W. performed the simulation; B.C., H.W., Y.C., and K.C. completed data analysis and figure depicture; B.C., H.W., and Y.H. wrote and revised the paper and J.L., D.W., J.C., and Y.H. supervised the project.

Data Availability Statement

The data that support the findings of this study are available from the corresponding author upon reasonable request.

Keywords

cooperative interactions, femtosecond laser, high movement velocity, non-contact manipulation

Received: November 11, 2024
Revised: February 10, 2025
Published online:

[1] H. Xu, S. Wu, Y. Liu, X. Wang, A. K. Efremov, L. Wang, J. S. McCaskill, M. Medina-Sánchez, O. G. Schmidt, *Nat. Nanotechnol.* **2024**, *19*, 494.
[2] R. Dreyfus, Q. Boehler, S. Lyttle, P. Gruber, J. Lussi, C. Chautems, S. Gervasoni, J. Berberat, D. Seibold, N. Ochsenbein-Kölble, M. Reinehr, M. Weisskopf, L. Remonda, B. J. Nelson, *Sci. Robot.* **2024**, *9*, eadh0298.
[3] J. Wu, N. Jiao, D. Lin, N. Li, T. Ma, S. Tung, W. Cheng, A. Wu, L. Liu, *Adv. Mater.* **2024**, *36*, 2306876.
[4] N. Li, P. Fei, C. Tous, M. Rezaei Adariani, M.-L. Hautot, I. Ouedraogo, A. Hadjadj, I. P. Dimov, Q. Zhang, S. Lessard, Z. Nosrati, C. N. Ng, K. Saatchi, U. O. Häfeli, C. Tremblay, S. Kadoury, A. Tang, S. Martel, G. Soulez, *Sci. Robot.* **2024**, *9*, eadh8702.
[5] X. Tang, Y. Yang, M. Zheng, T. Yin, G. Huang, Z. Lai, B. Zhang, Z. Chen, T. Xu, T. Ma, H. Pan, L. Cai, *Adv. Mater.* **2023**, *35*, 2211509.
[6] G. T. Iványi, B. Nemes, I. Gróf, T. Fekete, J. Kubacková, Z. Tomori, G. Bánó, G. Vizsnyiczai, L. Kelemen, *Adv. Mater.* **2024**, *36*, 2401115.
[7] G. Lucarini, V. Iacovacci, P. J. Gouveia, L. Ricotti, A. Menciassi, *J. Micromech. Microeng.* **2018**, *28*, 025009.
[8] S. Fusco, H.-W. Huang, K. E. Peyer, C. Peters, M. Häberli, A. Ulbers, A. Spyrogianni, E. Pellicer, J. Sort, S. E. Pratsinis, B. J. Nelson, M. S. Sakar, S. Pané, *ACS Appl. Mater. Interfaces* **2015**, *7*, 6803.
[9] B. Wang, Y. Chen, Y. Wang, F. Ji, H. Li, S. Niu, Z. Han, Y. Zhang, Z. Guo, *Sci. China Technol. Sci.* **2024**, *67*, 2164.
[10] H. Zhang, L. Meng, Y. Zhang, Q. Xin, Y. Zhou, Z. Ma, L. Zuo, C. Zheng, J. Luo, Y. Zhou, C. Ding, J. Li, *Adv. Mater.* **2024**, *36*, 2311446.
[11] R. Bernasconi, D. Carniani, M.-S. Kim, S. Pané, L. Magagnin, *ACS Appl. Mater. Interfaces* **2023**, *15*, 2396.
[12] H. Wu, J. Luo, X. Huang, L. Wang, Z. Guo, J. Liang, S. Zhang, H. Xue, J. Gao, *J. Colloid Interface Sci.* **2021**, *603*, 282.
[13] M. Tan, P. Tian, Q. Zhang, G. Zhu, Y. Liu, M. Cheng, F. Shi, *Nat. Commun.* **2022**, *13*, 5201.
[14] N. Bowden, A. Terfort, J. Carbeck, G. M. Whitesides, *Science* **1997**, *276*, 233.
[15] A. Barbot, H. Tan, M. Power, F. Seichepine, G.-Z. Yang, *Sci. Robot.* **2019**, *4*, eaax8336.
[16] A. Pena-Francesch, J. Giltinan, M. Sitti, *Nat. Commun.* **2019**, *10*, 3188.
[17] F. N. Piñan Basualdo, A. Bolopion, M. Gauthier, P. Lambert, *Sci. Robot.* **2021**, *6*, eabd3557.
[18] Y. Xiang, B. Li, B. Li, L. Bao, W. Sheng, Y. Ma, S. Ma, B. Yu, F. Zhou, *ACS Appl. Mater. Interfaces* **2022**, *14*, 20291.
[19] Z. Hu, W. Fang, Q. Li, X.-Q. Feng, J.-a. Lv, *Nat. Commun.* **2020**, *11*, 5780.
[20] J. Yuan, J. Feng, S. K. Cho, *Micromachines* **2021**, *12*, 341.
[21] J. M. Carballo, Q. Ni, J. Vasquez, N. B. Crane, *Colloids Surf. A Physicochem. Eng. Asp.* **2017**, *512*, 118.
[22] Y. Chen, N. Doshi, B. Goldberg, H. Wang, R. J. Wood, *Nat. Commun.* **2018**, *9*, 2495.
[23] Z. Li, N. V. Myung, Y. Yin, *Sci. Robot.* **2021**, *6*, eabi4523.
[24] A. Sepúlveda, D. Boudreau, *ACS Appl. Polym. Mater.* **2024**, *6*, 2359.
[25] J. Huang, X. Yu, L. Li, W. Wang, H. Zhang, Y. Zhang, J. Zhu, J. Ma, *ACS Nano* **2024**, *18*, 2006.
[26] Y. He, L. Wang, Q. Li, W. Rong, L. Sun, L. Yang, *J. Micromech. Microeng.* **2019**, *29*, 025010.

 © 2025 Wiley-VCH GmbH

15214095, 0, Downloaded from https://advanced.onlinelibrary.wiley.com/doi/10.1002/adma.202417416 by University Of Science, Wiley Online Library on [21/02/2025]. See the Terms and Conditions (https://onlinelibrary.wiley.com/terms-and-conditions) on Wiley Online Library for rules of use; OA articles are governed by the applicable Creative Commons License

[27] G. Gardi, S. Ceron, W. Wang, K. Petersen, M. Sitti, *Nat. Commun.* **2022**, *13*, 2239.
[28] W. Wang, G. Gardi, P. Malgaretti, V. Kishore, L. Koens, D. Son, H. Gilbert, Z. Wu, P. Harwani, E. Lauga, C. Holm, M. Sitti, *Sci. Adv.* **2022**, *8*, eabk0685.
[29] Y. He, L. Wang, K. Yang, X. Wang, W. Rong, L. Sun, *ACS Appl. Mater. Interfaces* **2021**, *13*, 46180.
[30] X. Wang, D. Lin, Y. Zhou, N. Jiao, S. Tung, L. Liu, *ACS Nano* **2022**, *16*, 14895.
[31] L. Su, D. Jin, Y. Wang, Q. Wang, C. Pan, S. Jiang, H. Yang, Z. Yang, X. Wang, N. Xia, K. F. Chan, P. W. Y. Chiu, J. J.-Y. Sung, L. Zhang, *Sci. Adv.* **2023**, *9*, eadj0883.
[32] M. Sun, S. Yang, J. Jiang, S. Jiang, M. Sitti, L. Zhang, *Sci. Adv.* **2023**, *9*, eadj4201.
[33] B. Wang, K. F. Chan, K. Yuan, Q. Wang, X. Xia, L. Yang, H. Ko, Y.-X. J. Wang, J. J. Y. Sung, P. W. Y. Chiu, L. Zhang, *Sci. Robot.* **2021**, *6*, eabd2813.
[34] J. Li, X. Li, T. Luo, R. Wang, C. Liu, S. Chen, D. Li, J. Yue, S.-h. Cheng, D. Sun, *Sci. Robot.* **2018**, *3*, eaat8829.
[35] Y. He, L. Wang, M. Zhao, Z. Fan, W. Rong, L. Sun, *ACS Appl. Mater. Interfaces* **2022**, *14*, 22570.
[36] J. Kim, S. E. Chung, S.-E. Choi, H. Lee, J. Kim, S. Kwon, *Nature Mater* **2011**, *10*, 747.
[37] C. Chen, S. Ding, J. Wang, *Nat. Rev. Mater.* **2024**, *9*, 159.
[38] B. Wang, D. Liu, Y. Liao, Y. Huang, M. Ni, M. Wang, Z. Ma, Z. Wu, Y. Lu, *ACS Nano* **2022**, *16*, 20985.
[39] H. Kwon, Y. Yang, G. Kim, D. Gim, M. Ha, *Nanoscale* **2024**, *16*, 6778.
[40] C. Zeng, M. W. Faaborg, A. Sherif, M. J. Falk, R. Hajian, M. Xiao, K. Hartig, Y. Bar-Sinai, M. P. Brenner, V. N. Manoharan, *Nature* **2022**, *611*, 68.
[41] M. S. Wo, R. U. Gobithaasan, K. T. Miura, K. C. Loy, F. N. Harun, *Mathematics* **2023**, *11*, 103.
[42] H. Bai, P. Li, X. Wang, Z. Li, T. Zhao, Y. Tian, M. Cheng, Y. Hong, X. Zhu, M. Cao, *Adv. Funct. Mater.* **2024**, *34*, 2400574.
[43] M. Nosonovsky, B. Bhushan, *Microsyst. Technol.* **2005**, *11*, 535.
[44] A. F. Molland, S. R. Turnock, D. A. Hudson, in *Ship Resistance and Propulsion: Practical Estimation of Propulsive Power*, Cambridge University Press, Cambridge **2011**.
[45] K. Hou, D. Guan, H. Li, Y. Sun, Y. Long, K. Song, *Sci. Adv.* **2021**, *7*, eabh3051.
[46] T. M. Barbosa, R. Ramos, A. J. Silva, D. A. Marinho, *J. Sports Sci.* **2018**, *36*, 492.
[47] M. Testa-Anta, S. Liébana-Viñas, B. Rivas-Murias, B. R. González, M. Farle, V. Salgueiriño, *Nanoscale* **2018**, *10*, 20462.
[48] J. Lipfert, X. Hao, N. H. Dekker, *Biophys. J.* **2009**, *96*, 5040.
[49] C. W. Extrand, S. I. Moon, *Langmuir* **2009**, *25*, 992.
[50] X. Dong, M. Sitti, *Int. J. Rob. Res.* **2020**, *39*, 617.

© 2025 Wiley-VCH GmbH

15214095, 0, Downloaded from https://advanced.onlinelibrary.wiley.com/doi/10.1002/adma.202417416 by University Of Science, Wiley Online Library on [21/02/2025]. See the Terms and Conditions (https://onlinelibrary.wiley.com/terms-and-conditions) on Wiley Online Library for rules of use; OA articles are governed by the applicable Creative Commons License